Xu *et al. Microstructures* **2025**, *5*, 2025089
DOI: 10.20517/microstructures.2024.143

Microstructures

Research Article

Open Access

Ameliorating the microstructure and mechanical properties of Al-Cu-Li alloy through aging temperature in a novel thermo-mechanical treatment

Xuanxi Xu, Xin Tong, Guohua Wu, Liang Zhang

National Engineering Research Center of Light Alloy Net Forming and State Key Laboratory of Metal Matrix Composites, School of Materials Science and Engineering, Shanghai Jiao Tong University, Shanghai 200240, China.

Correspondence to: Dr. Xin Tong and Prof. Guohua Wu, National Engineering Research Center of Light Alloy Net Forming and State Key Laboratory of Metal Matrix Composites, School of Materials Science and Engineering, Shanghai Jiao Tong University, 800 Dongchuan Road, Minhang District, Shanghai 200240, China. E-mails: xintong@sjtu.edu.cn; ghwu@sjtu.edu.cn

How to cite this article: Xu, X.; Tong, X.; Wu, G.; Zhang, L. Ameliorating the microstructure and mechanical properties of Al-Cu-Li alloy through aging temperature in a novel thermo-mechanical treatment. *Microstructures* **2025**, *5*, 2025089. https://dx.doi.org/10.20517/microstructures.2024.143

Received: 2 Dec 2024 **First Decision:** 18 Feb 2025 **Revised:** 8 Mar 2025 **Accepted:** 12 Mar 2025 **Published:** 12 Aug 2025

Academic Editor: Xiaozhou Liao **Copy Editor:** Shu-Yuan Duan **Production Editor:** Shu-Yuan Duan

Abstract

Developing wrought aluminum-lithium alloys with high strength and ductility has been a longstanding objective in the aviation and aerospace industry. However, the conventional T8 thermo-mechanical treatment process faces challenges in overcoming the strength-ductility compromise in aluminum-lithium alloys. The precipitates-dislocation interaction is critical in governing the balance between strength and ductility. When the aging temperature exceeds 175 °C, the T_1 phase thickens, making it difficult for slip dislocations to shear the coarser T_1 phase. This results in severe matrix distortion near the precipitates, thereby reducing ductility. In contrast, aging at 150 °C promotes the formation of fine, shearable T_1 phases, facilitating uniform plastic deformation across multiple slip planes and achieving a balance of high strength (~ 705 MPa) and ductility (~ 11.8%). Aging at 120 °C further improves ductility (~ 12.4%) due to the coexistence of sparse T_1 phases and large amounts of Guinier-Preston (GP) zones, which promoted dislocation cross-slip. Our findings highlight the critical importance of precisely controlling the relative amount, size, and distribution of GP zones and T_1 precipitates to achieve superior mechanical performance in Al-Cu-Li-Mg-Ag alloys.

Keywords: Al-Cu-Li alloy, precipitation, microstructure, mechanical properties

INTRODUCTION

The high strength-to-weight ratio and stiffness of Al-Cu-Li-based alloys have made them a focus of interest for aerospace applications[1,2]. Recent research has focused on improving the balance between the strength and ductility of wrought lightweight alloys, especially for Al-Cu-Li-based alloys[3-6]. The conventional T8 thermo-mechanical treatment (TMT) process, involving pre-stretching followed by artificial aging, is widely used to relieve quench-induced stress and promote the formation of strengthening precipitates through dislocation generation[7-10]. However, this approach often leads to a notable reduction in plasticity. This decline is primarily attributed to local stress concentrations caused by the migration of dislocations to grain boundaries (GBs) in the as-quenched matrix after pre-stretching, resulting in uneven precipitation[11,12]. Rodgers *et al.*[13] demonstrated that increasing the pre-stretching level in the AA2195 alloy from 3% to 15% improved the yield strength (YS) to 670 MPa but reduced elongation (EL) from 11% to 7.5%. Similarly, Huang *et al.*[14] reported that ~ 8% pre-stretching decreased the EL of Al-Cu-Mg alloys to 7.3%.

To promote dense and homogeneous precipitation in Al-Cu-Li alloys subjected to pre-stretching, two main strategies have been proposed: (1) Low-level pre-stretching (0%-3%) prior to artificial aging: This approach aims to reduce dislocation entanglement and create heterogeneous nucleation sites for the T_1 precipitate. However, the resulting improvements in strength and ductility remain limited; (2) Cryogenic-temperature pre-stretching: Pre-stretching at cryogenic temperatures has been shown to enhance grain deformation, potentially promoting uniform dislocation distribution and improving T_1 nucleation[15-17]. Nevertheless, the practical application of this method is constrained by its limited industrial feasibility; (3) Thermos-mechanical treatment combined with pulsed electromagnetic field treatment (PEFT): Pre-stretching followed by PEFT regulates dislocation behavior through magnetically induced stress[18,19]. The stress field generated by magnetostriction provides effective driving forces for homogeneous dislocation migration, leading to the formation of uniform dislocation networks[18]. This optimized defect configuration facilitates the homogeneous precipitation of fine, dispersed T_1 phases during subsequent artificial aging. However, the strong eddy currents induced by PEFT rapidly elevate the alloy's temperature, pushing it into the static recovery regime[18]. This thermal activation triggers static recovery of high-density dislocations, reducing dislocation density and, consequently, diminishing the strain-strengthening effect.

Our previous work introduced an innovative TMT in Al-Cu-Li-Mg-Ag alloys, incorporating a low-temperature pre-aging step before pre-stretching to promote the formation of metastable Guinier-Preston (GP) zones[20,21]. This approach mitigates localized stress concentrations caused by dislocation entanglement during pre-stretching, leading to a more even dislocation structure at up to 8% pre-stretching and enabling a homogeneous precipitate distribution. In age-hardening alloys, optimizing precipitation behavior through controlled dislocation configuration and tailored heat treatment is crucial for achieving superior mechanical properties. The primary precipitates in Al-Cu-Li alloys include T_1 (Al_2CuLi) and θ' (Al_2Cu), with δ' (Al_3Li), S' (Al_2CuMg) phases, and δ'/GP zone/δ' composite precipitates also occasionally present within the matrix[22,23]. Among these, T_1 phases, characterized by their high aspect ratio and formation on the $\{111\}_{Al}$ habit plane, are the most effective strengthening phases due to their thin platelet structure, which impedes dislocation motion. The simultaneous improvement of strength and ductility in Al-Cu-Li alloys is primarily governed by dynamic interactions between mobile dislocations and precipitates, which can be modulated through precise aging treatments[21,24,25].

In the under-aged Al-Cu-Li alloy, fine T_1 phases and GP zones serve as shearable precipitates, which eventually evolve into shear-resistant, large-diameter T_1 and θ' precipitates at peak aging[26]. Shear-resistant precipitates interact with dislocations, which leads to the formation of Orowan loops around the precipitates, significantly increasing local stress and enhancing alloy strength. However, the emergence of

microvoids at the interface between precipitates and the matrix leads to reduced ductility[27,28]. The aging temperature plays a critical role in governing both precipitation kinetics and mechanical properties in Al-Cu-Li alloys. Cui *et al.*[29] systematically investigated the precipitation behavior in an Al-4Cu-1Li-0.5Mg-0.4Ag alloy during isothermal aging (155-185 °C). Microstructural analysis revealed temperature-dependent precipitation sequences: the T_1 phase predominated at 155 °C, with suppressed formation of θ' and S' phases. At 185 °C, accelerated nucleation of θ', S', and σ ($Al_5Cu_6Mg_2$) phases enhanced strength but reduced plasticity. As aging temperatures exceeded 200 °C, T_1 phase coarsening at GBs, along with precipitation-free zone (PFZ) formation, became the primary contributors to plasticity degradation[30]. Understanding the complex precipitation behavior and the resulting microstructure in TMT samples, particularly its dependence on aging temperature, is essential. Further investigation is therefore needed to elucidate the influences of aging treatment on precipitation behavior and mechanical properties in Al-Cu-Li-Mg-Ag alloys subjected to pre-aging and 8% pre-stretching.

The objective of this study is to explore the possibility of enhancing the balance between strength and ductility in Al-Cu-Li-Mg-Ag alloy by utilizing a combination of precipitates and dislocations. An extruded Al-Cu-Li-Mg-Ag alloy undergoes pre-aging at 110 °C, followed by 8% pre-stretching and post-aging at 120-200 °C for varying durations to achieve tailored combinations of dislocations and precipitates. Thorough microscopic characterization and mechanical property analysis are performed to elucidate the competitive interactions between precipitates and dislocations, offering new insights into the design of high-performance extruded Al-Cu-Li-based samples.

EXPERIMENTAL METHODS

The ingots were fabricated using the gravity permanent mold casting method. The actual composition of the ingots, determined by inductively coupled plasma optical emission spectrometry (ICP-OES), was Al-3.7Cu-1.0Li-0.4Mg-0.8Ag-0.4Mn-0.1Zr (wt.%). After two-step homogenization at 500 °C for 10 h and 515 °C for 20 h, the alloy was hot-extruded into rods at 440 °C with an extrusion ratio of 25:1. The extruded rods were rapidly cooled in water at room temperature and then solution treated at 530 °C for 90 min using a chamber electric furnace. To achieve a homogeneous dislocation distribution[21], the as-quenched sample underwent a low pre-aging treatment at 110 °C for 4 h immediately after solution treatment, with the entire process from solution treatment to pre-aging taking less than 5 min. Subsequently, an 8% pre-strain was applied along the extrusion direction using a Zwick/Roell Z100 testing machine. The pre-stretched sample was then aged at 120 °C, 150 °C, 175 °C, and 200 °C in an oil bath furnace until peak aging was reached. A schematic flow diagram of the processing procedures is shown in Figure 1, with abbreviations for the four TMT processes summarized in Table 1.

The microscale structure of the samples was characterized using optical microscopy (OM, LEICA MEF4M) and scanning electron microscopy (SEM, NOVA NanoSEM 230, FEI) equipped with a backscattered electron detector (BSE) and energy-dispersive X-ray spectroscopy (EDS). Transmission electron microscopy (TEM) specimens were prepared using a twin-jet electro-polishing unit with an electrolyte consisting of 30 vol.% nitric acid and 70 vol.% methanol at -30 °C. TEM observations were conducted on a Thermo-Fisher Talos scanning transmission electron microscope (STEM) operating at 200 kV to characterize the nano-precipitates. Dislocation structures were observed in bright-field TEM (BF-TEM) mode, while imaging of Cu-containing precipitates was performed using high-angle annular dark-field scanning transmission electron microscopy (HAADF-STEM) in atomic number contrast mode. The thickness of precipitates was observed using high-resolution TEM (HRTEM). The samples for TEM observation were mechanically ground to approximately 65 μm and then electropolished at 25 V in a 4 vol.% perchloric acid ethanol solution at -25 °C. The diameter and number density of different precipitates on the $(112)_{Al}$ and $(110)_{Al}$

Table 1. The abbreviations of the TMT process involved in the study

Abbreviations	Solution treatment	Pre-treatment	Aging treatment
TMT-120	530 °C/1.5 h	110 °C/4 h + 8% pre-stretching	120 °C/100 h
TMT-150	530 °C/1.5 h	110 °C/4 h + 8% pre-stretching	150 °C/20 h
TMT-175	530 °C/1.5 h	110 °C/4 h + 8% pre-stretching	175 °C/8 h
TMT-200	530 °C/1.5 h	110 °C/4 h + 8% pre-stretching	200 °C/4 h

TMT: Thermo-mechanical treatment.

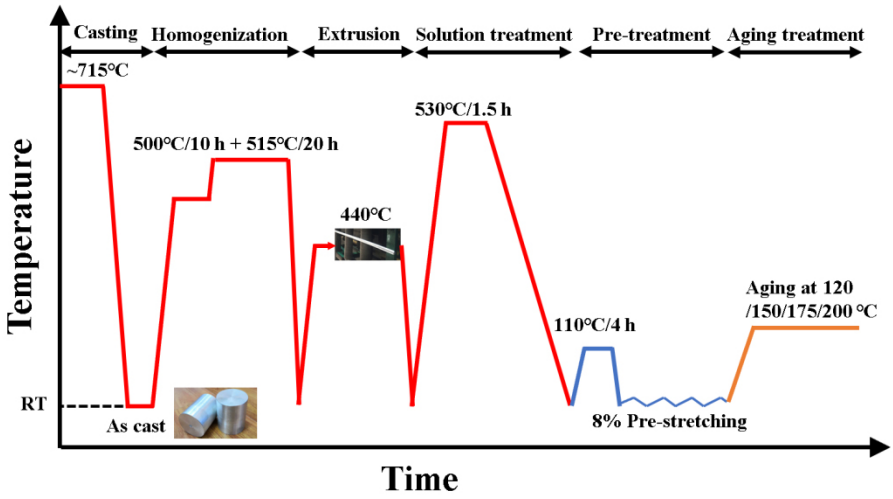

Figure 1. Schematic flow diagram of the processing procedures for the alloys.

planes were measured from at least three HAADF images using Image-Pro Plus 6.0 software. To determine the number density (N) and volume fraction (f_v) of T_1 and θ' precipitates, the thickness (t) of the TEM foils was measured using convergent beam electron diffraction (CBED), a technique known for its high accuracy[31]. The thickness of the TEM foil was determined to be 179.9 nm based on our previous findings[21], and it was reasonably assumed to remain consistent across all samples, as supported by other researchers[13]. The f_v of the platelet T_1 and θ' phases is defined as[32]:

$$f_v = \frac{\pi N D^2 t}{4} \quad (1)$$

Where N, D, and t are the number density, diameter, and thickness of the precipitates, respectively. The number density (N) is calculated by[32]:

$$N = \frac{n}{x \times y \times t_{foil}} \quad (2)$$

Where x and y are the dimensions of the HAADF-STEM images, t_{foil} is the thickness of the TEM foil.

Microhardness and tensile tests were conducted to evaluate the mechanical properties of the alloys at different aging temperatures. Hardness measurements were performed using a Vickers hardness tester (XHVT-1000Z, SCTMC) with a 49 N load and a dwell time of 15 s, with at least five indentations to ensure statistical accuracy. Room-temperature tensile properties were tested using a 100 KN electronic universal testing machine (Z100, Zwick/Roell) with a tensile speed of 0.9 mm/min. Tensile samples were prepared in

a flat dog-bone shape, with a gauge section of 15.0 mm (length) × 3.5 mm (width) × 2.0 mm (thickness). To ensure measurement accuracy, triplicate tensile specimens were evaluated under each TMT sample, with mean values derived from the collected data.

RESULTS AND DISCUSSION

Initial microstructure

Figure 2A presents the OM image of the as-cast microstructure, which predominantly consists of dendritic α-Al grains, with intermetallic phases distributed along the GBs. The BSE image in Figure 2B reveals a network structure of secondary phases around the GBs, suggesting the need for further heat treatment to eliminate elemental segregation. Figure 2C displays enlarged microstructural images of the as-cast alloys. EDS mapping in Figure 2D shows that the continuous dendrites are mainly enriched with Cu, with a slight enrichment in Ag. Composition profiles along line 1 crossing the secondary phases reveal the presence of Al, Cu, and Ag, while the Mg element was undetectable [Figure 2E]. Based on earlier research, the intermetallic phases rich in Cu at the GBs are likely to be equilibrium phases, such as the T_B (Al_7Cu_4Li), T_2 (Al_6CuLi_3), and S (Al_2CuMg) phases[33].

The microstructure of the Al-Cu-Li alloys after homogenization treatments is shown in Figure 3. Following the two-step homogenization treatments, a notable decrease in the size of the coarse dendritic structures is observed in the original as-cast alloy [Figure 3A]. The BSE images of the homogenized alloys reveal that most Cu-containing phases have dissolved into the α-Al matrix [Figure 3B]. EDS analysis revealed that the residual secondary phases after homogenization treatment are primarily identified as Al-Cu and Al-Cu-Mn-Fe phases [Figure 3B and C]. Typically, the rod-like $Al_{20}Cu_2Mn_3$ phase with micrometer size precipitates during homogenization[34]. Therefore, the residual secondary phases are likely to be insoluble Cu-containing phases and $Al_{20}Cu_2Mn_3$ phases. Additionally, due to the low Zr content (0.1 wt.%) in the Al-Cu-Li alloy, only a few Al_3Zr phases precipitated during homogenization can be observed [Figure 3C]. These nanoscale Al_3Zr phases effectively pin grain boundaries, inhibiting recrystallization during hot deformation[34]. The residual secondary phases have become discrete and smaller, indicating that the two-stage homogenization effectively eliminated grain interior segregation.

Figure 4 displays the OM images and corresponding BSE images of the alloy after extrusion and solution treatment. The as-extruded alloy exhibits grains with a mean thickness of 65.3 μm, showing significant compression and elongation, and a fibrous morphology [Figure 4A]. Additionally, large amounts of Cu-enriched secondary phases are observed reprecipitating along the GBs, as shown in the BSE image in Figure 4B. The formation of the Cu-containing secondary phase during the hot extrusion reduces the supersaturation of the matrix, requiring further solid solution treatment. After solution treatment, the grain morphology and average thickness remain nearly unchanged [Figure 4C], suggesting that recrystallization does not occur significantly during the solution treatment. The addition of Zr to the alloy promotes the uniform precipitation of Al_3Zr particles during homogenization, which significantly impedes the movement of GBs, thereby inhibiting recrystallization in the solution-treated alloy[35]. Additionally, after solution treatment, the clear GB morphology indicates that most of the particles have redissolved into the matrix [Figure 4D].

Effect of pre-treatment on dislocation configuration

Figure 5A and B exhibit the BF-TEM image of the Al-Cu-Li alloy after solution treatment, with the electron beam along the $[110]_{Al}$ zone. For the as-quenched alloy [Figure 5B], straight and closely arranged helical dislocation lines are observed, though they are unevenly distributed. However, for the as-quenched alloy subjected directly to 8% pre-stretching [Figure 5C], a substantial amount of unevenly distributed

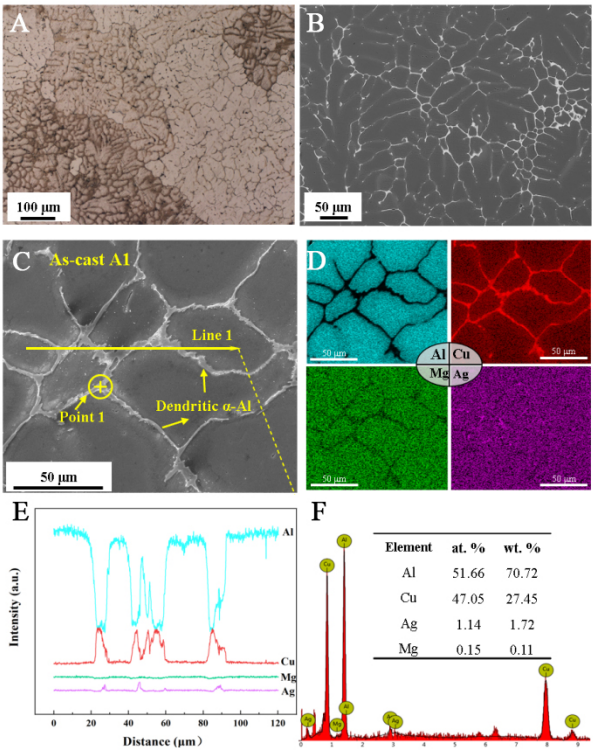

Figure 2. Microstructure of as-cast alloy:(A) Optical micrographs; (B and C) SEM backscattered electron; (D) EDS mapping in Figure 2C; EDS line scanning in Figure 2C; (F) EDS spot scanning of point 1 in Figure 2C. SEM: Scanning electron microscopy; EDS: X-ray spectroscopy.

dislocations, including dislocation cells and dense dislocation zones, are present within the matrix [Figure 5D], indicating significant dislocation entanglement after high pre-stretching. In contrast, a homogeneous, high-density dislocation configuration is achieved through a novel pre-treatment process [Figure 5E and F], which involves low-temperature pre-aging at 110 °C followed by 8% pre-stretching. The selected area diffraction pattern (SADP) in Figure 5E reveals slight streaks along the <100> directions, which are identified as GP zones. These metastable GP zones, which serve as precursors to the θ' precipitate, are fully coherent with the Al matrix and reside on the {100} matrix planes[36]. As a result, the high density of metastable GP zones that form during low-temperature pre-aging effectively alleviates dislocation entanglement during pre-stretching [Figure 5F]. Hence, under the same 8% pre-stretching, the GP zones formed during pre-aging contribute to a more uniform dislocation distribution. Although some dislocation tangling inevitably occurs in the matrix, the dislocation structure in the TMT sample remains more uniform compared to the as-quenched sample subjected to 8% pre-stretching. GP zones are widely recognized as thermodynamically metastable, characterized by weak interactions between solutes[37]. The interactions between dislocations and metastable GP zones can induce atomic rearrangement, separation, and dissolution within the GP zones, thereby reducing local stress and strain concentrations during pre-stretching[12,38]. As a result, large amounts of fine GP zones can effectively inhibit dislocation motion. Multiple interactions between dislocations and GP zones increase the dislocation mean free path[21], leading to a more even dislocation structure, even under a high pre-stretching level of 8%, as observed in this study. Furthermore, Chen *et al.*[39] reported that the dissolution of fine GP zones during tensile deformation not only enhances strain hardening but also promotes the redistribution of Cu solutes into the matrix, which positively influences the plasticity of the Al matrix.

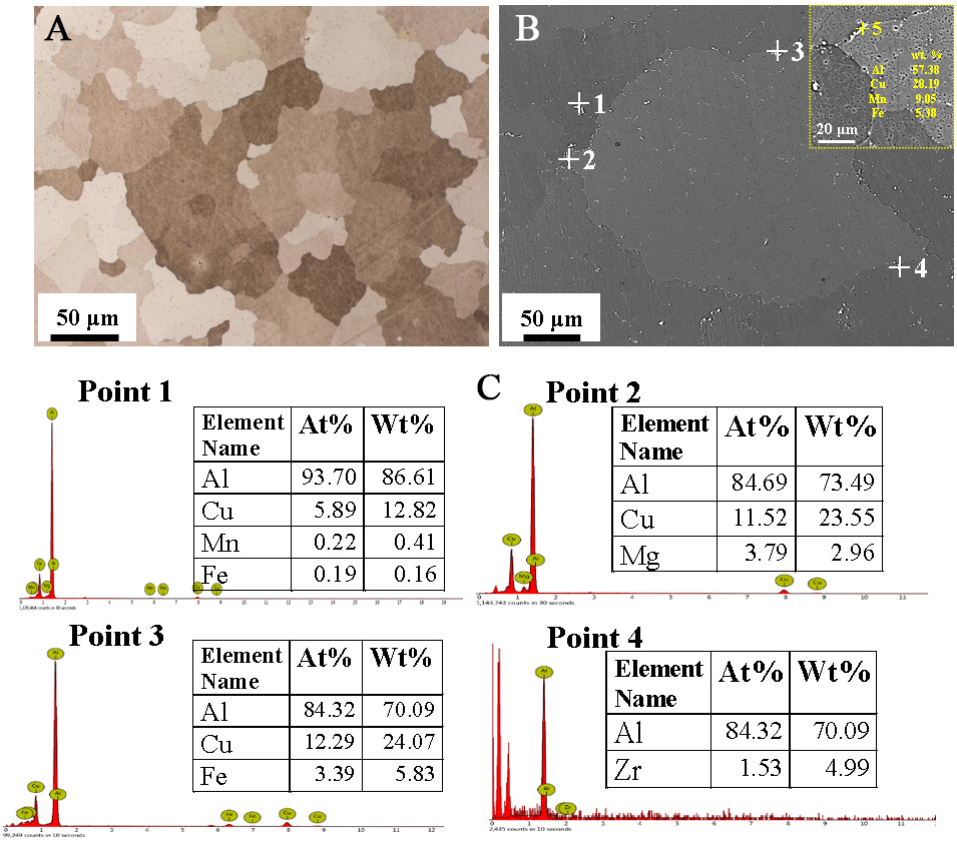

Figure 3. Microstructure of homogenized alloy: (A) OM image; (B) BSE image (the yellow dotted line indicates the area of higher magnification); (C) EDS spot scanning analysis of Figure 3B. OM: Optical microscopy; BSE: backscattered electron detector; EDS: X-ray spectroscopy.

Age-hardening response

Figure 6A presents the age-hardening response of TMT samples aged at 120 °C, 150 °C, 175 °C, and 200 °C. The statistical results of peak-aged hardness and peak-aging times are displayed in Figure 6B. The hardness of the solution-treated sample is approximately 90 HV, which increases to about 119 HV after pre-aging at 110 °C. After 8% pre-stretching, the hardness further increases to approximately 144 HV. During artificial aging, the hardness of the TMT samples initially rises to a maximum value and then declines as the aging time is extended. The TMT-150 sample exhibits peak hardness at 150 °C after 20 h and maintains a plateau in hardness for up to 100 h [Figure 6B]. The maximum hardness for aging at 175 °C (205 HV) and 200 °C (191 HV) is nearly the same; however, the time to reach peak hardness declines greatly as the aging temperature rises, with the peak aging time reduced to 4 h at 200 °C. In contrast, when the aging temperature is reduced to 120 °C, the peak hardness reaches 189 HV after 100 h, indicating slower aging kinetics for the TMT-120 sample.

Effect of aging temperature on precipitation behavior

The precipitation behavior of peak-aged TMT samples under different aging temperatures was characterized using HAADF-STEM. Figure 7 presents TEM images and corresponding SADPs obtained with the electron beam aligned parallel to the $<112>_{\alpha}$ direction for the four samples. The SADPs clearly display long streaks associated with T_1 precipitates in the $[1\bar{1}1]$ direction [Figure 7A-D], indicating the presence of T_1 phases. Since the T_1 phase precipitates along the $\{111\}_{Al}$ habit planes, only T_1 can be observed along the $<112>_{Al}$ axis[40]. As shown in Figure 7E, the peak-aged TMT-120 sample exhibits fine T_1

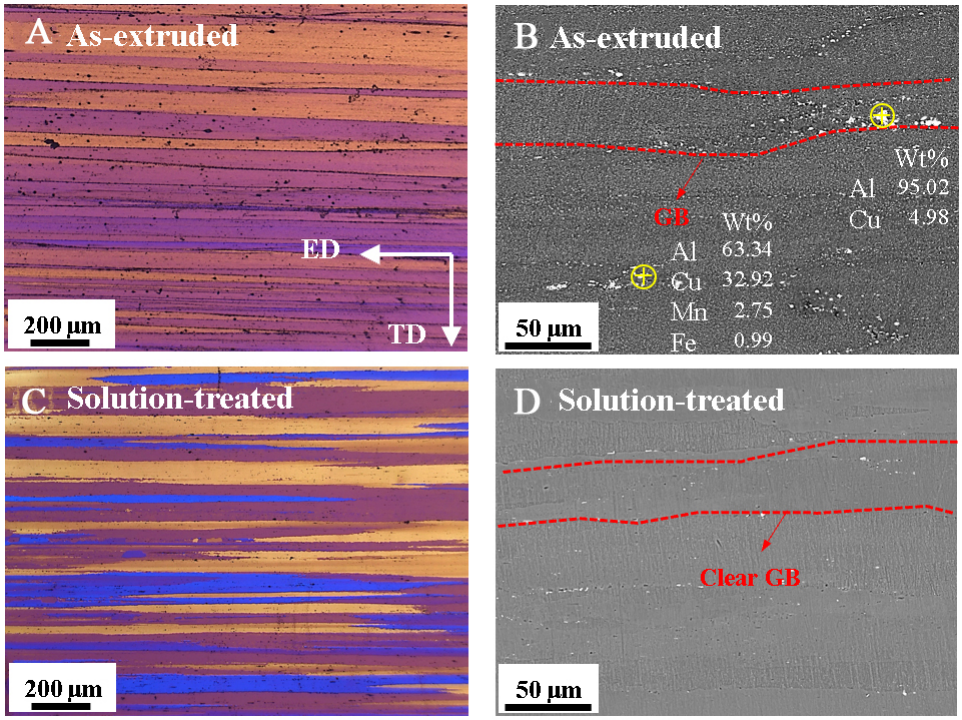

Figure 4. Microstructure of extruded alloy (A and B) and solution-treated alloy (C and D): OM image (A and C); BSE image (B and D). GB: Grain boundary; OM: optical microscopy; BSE: backscattered electron detector.ED: extrusion direction; TD: transverse direction.

precipitates uniformly distributed within the matrix. As the aging temperature is raised from 150 °C [Figure 7F] to 175 °C [Figure 7G], there is a notable increase in both the quantity and size of the T_1 phase, with the TMT-175 sample displaying the highest density of T_1 phases among all samples. However, further increasing the aging temperature to 200 °C, coarse T_1 phases appear in the microstructure [Figure 7H].

Figure 8 displays the SADPs and corresponding HAADF-STEM images of typical peak-aged samples along the $<110>_{Al}$ zone axis. This confirms that increasing the aging temperature facilitates heterogeneous nucleation on dislocations, which aligns with the results reported by Dong *et al.*[41]. In the SADPs, streaks in the [001] and [111] directions are associated with edge-on θ' and T_1 phases, respectively, while spots at $1/3\{022\}_\alpha$ represent inclined T_1 phases [Figure 8A-D]. It is important to note that, although a small amount of δ' and Al_3Zr phases also precipitate in the matrix [Figure 8], the Li content in the current alloy is intentionally designed low (≤ 1 wt.%) to minimize δ' phases formation[1,2], resulting in very limited precipitation of δ' phases. Additionally, Al_3Zr particles have minimal impact on the precipitation of the T_1 and θ' phases[13]. Therefore, this study focuses solely on the precipitation behavior of the primary strengthening phases, T_1 and θ'. In the TMT-120 sample, the intense streaks along the <100> direction indicate a higher number density of precipitates [Figure 8A]. These precipitates, with an average length of ~ 8 nm, are uniformly distributed in the matrix and identified as thin plate-shaped GP zones [Figure 8E], which are precursors of θ' phases lying on the {001} matrix planes. As the aging temperature increases from 150 °C [Figure 8F] to 175 °C [Figure 8G], GP zones are scarcely observed, accompanied by a reduction in streak intensity along the <100> direction in the SADPs. At 200 °C [Figure 8H], fine GP zones grow into coarse θ' phases at higher temperatures. In summary, varying aging temperatures affect the precipitation sequence in different TMT samples. At 120 °C, the precipitation sequence for the TMT-120 sample is as follows: SSS → GP zone + δ'/β' → GP zone + T_1. As the aging temperature increases from 150 °C to 200 °C, the precipitation sequence changes to: SSS → GP zone + δ'/β' → θ' + T_1.

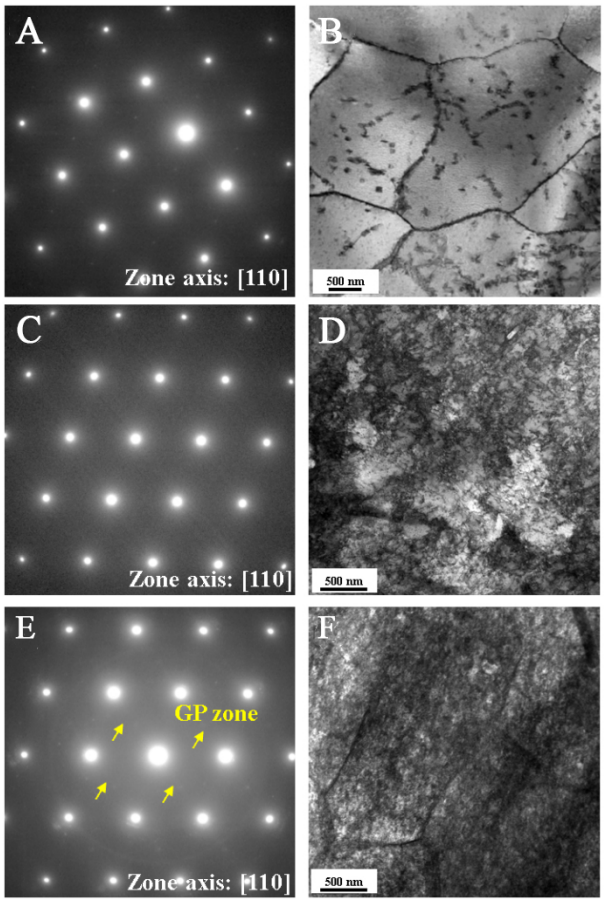

Figure 5. BF-TEM images (B, D and F) viewed along $[110]_{Al}$ zone axis and corresponding SADPs (A, C and E): as-quenched alloy (A, B); the as-quenched alloy direct subject to 8% pre-stretching (C, D); and the as-quenched alloy subjected to pre-aging and 8% pre-stretching (E and F). BF-TEM: Bright-field transmission electron microscopy; SADP: selected area diffraction pattern.

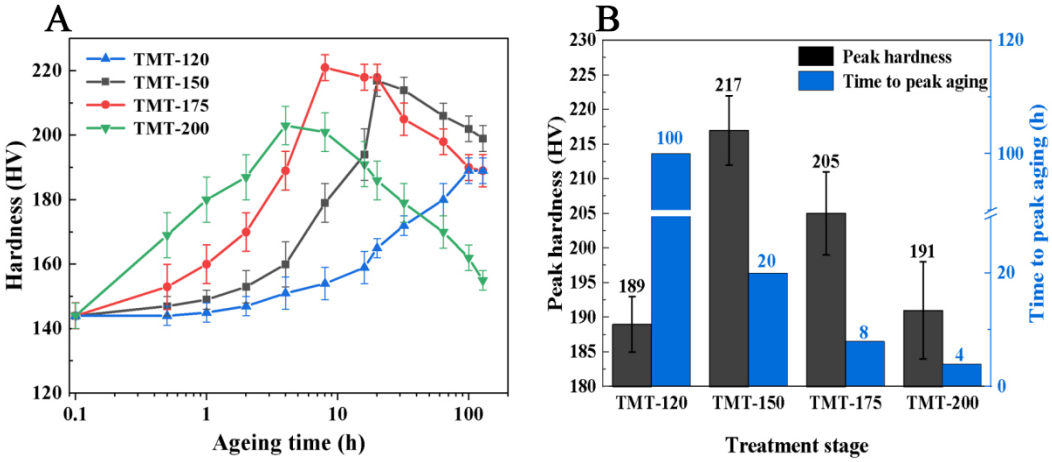

Figure 6. (A) Aging-hardening curves of the TMT samples aged at 120 °C, 150 °C, 175 °C, and 200 °C; (B) Peak-aging times and peak-aged hardness for different TMT samples. TMT: Thermo-mechanical treatment.

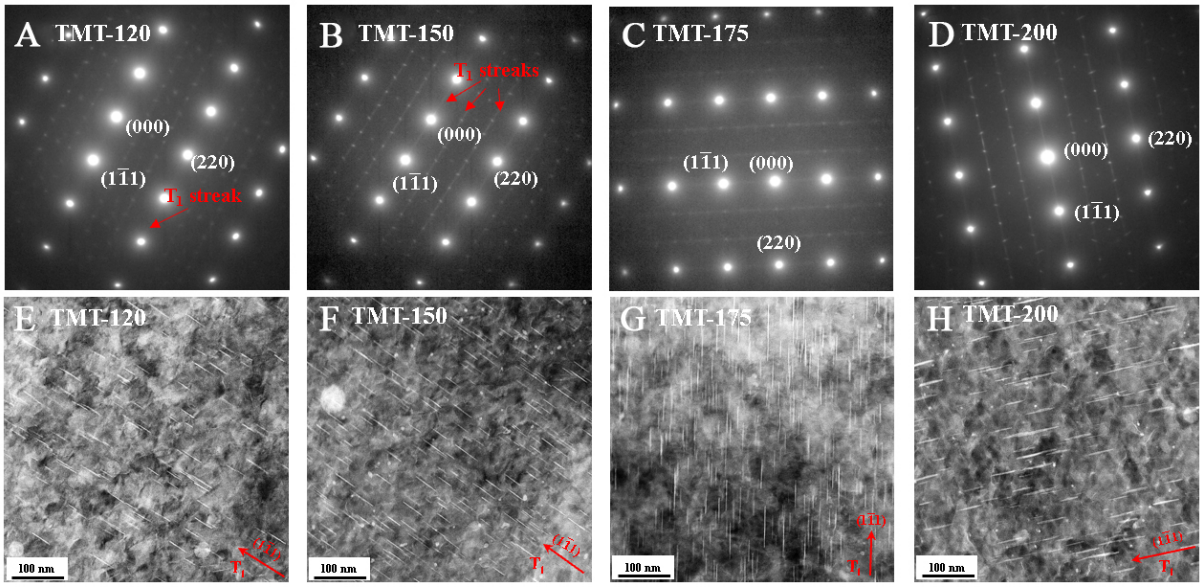

Figure 7. SADPs (A-D) and corresponding HAADF-STEM images (E-H) for the peak-aged samples viewed along the <112>$_\alpha$ direction: (A and E) TMT-120; (B and F) TMT-150; (C and G) TMT-175; (D and H) TMT-200. TMT: Thermo-mechanical treatment; SADP: selected area diffraction pattern; HAADF-STEM: high-angle annular dark-field scanning transmission electron microscopy.

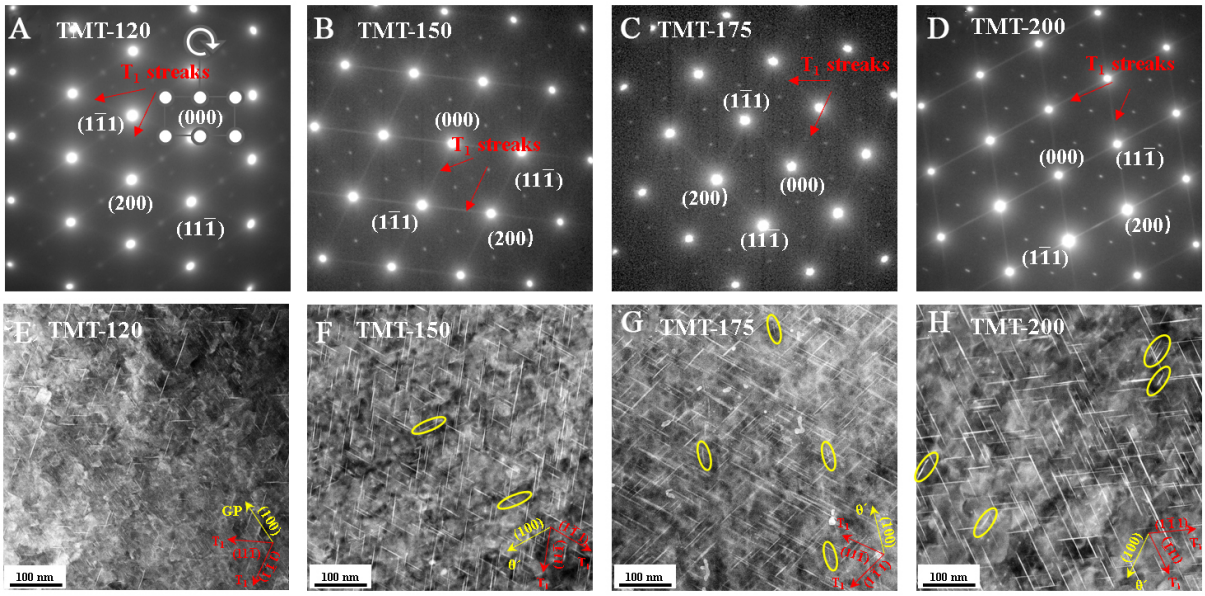

Figure 8. SADPs (A-D) and corresponding HAADF-STEM images (E-H) for the peak-aged samples viewed along the <110>$_\alpha$ direction: (A and E) TMT-120; (B and F) TMT-150; (C and G) TMT-175; (D and H) TMT-200. TMT: Thermo-mechanical treatment; SADP: selected area diffraction pattern; HAADF-STEM: high-angle annular dark-field scanning transmission electron microscopy.

Figure 9 illustrates the transformation of T_1 thickness in the TMT samples during peak aging. HRTEM images reveal a gradual increase in T_1 phase thickness, from 1.29 nm in the TMT-120 sample to 2.44 nm in the TMT-200 sample, as the aging temperature is raised from 120 °C to 200 °C [Figure 9A-D]. Notably, the TMT-120 sample exhibits the finest GP zone thickness (0.32 nm) and the thinnest T_1 phase (1.29 nm), as shown in Figure 9A.

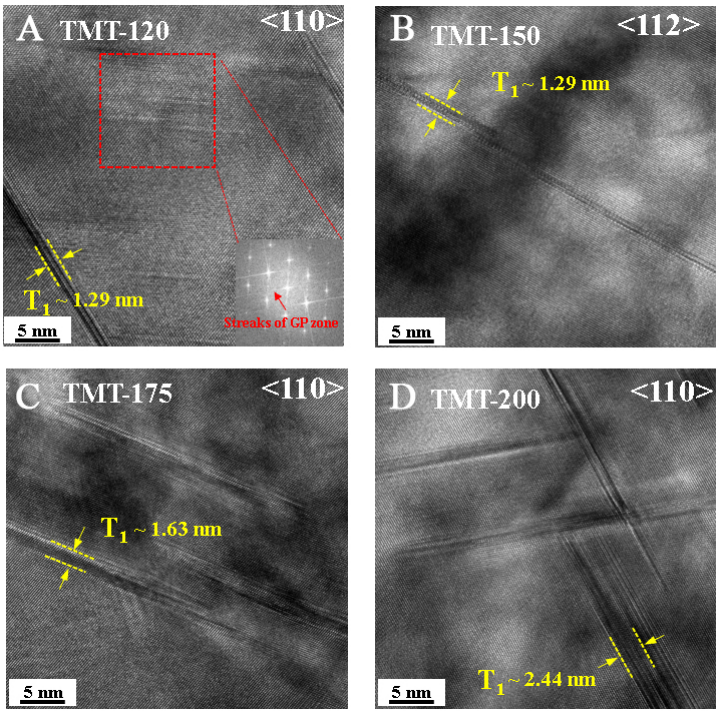

Figure 9. HRTEM images showing the thickness evolution of T_1 precipitates at peak aging: (A) TMT-120; (B) TMT-150; (C) TMT-175; (D) TMT-200. TMT: Thermo-mechanical treatment; HRTEM: high-resolution transmission electron microscopy.

The average diameter and number density of precipitates in different peak-aged samples are shown in Figure 10. Tables 2 and 3 list the measured precipitate parameters in observed HAADF-STEM images. The number density of the T_1 phase first rises and then declines as the aging temperature rises from 120 °C (TMT-120) to 200 °C (TMT-200), as shown in Figure 10A-D. In contrast, the number density of the θ' phase consistently declines with increasing temperature [Figure 10E-H], while its diameter increases to 30 nm [Figure 10F] before decreasing slightly to 25 nm [Figure 10G]. This trend reflects competitive precipitation between the T_1 and θ' phases, as both rely on Cu atoms for formation. At 120 °C, the TMT-120 sample shows smaller T_1 phases and GP zones, with the number density of GP zones (148×10^{21} m^{-3}) notably exceeding that of T_1 phases (3.2×10^{21} m^{-3}). Conversely, in the TMT-175 sample, the number density of θ' phases (1.4×10^{21} m^{-3}) is substantially lower than that of T_1 phases (5.6×10^{21} m^{-3}). These results highlight the effect of aging temperature on the competing precipitation behavior and the growth dynamics of the T_1 and θ' precipitates.

It is evident that aging temperature significantly affects the microstructure evolution of the T_1 and θ' precipitates. At the low aging temperature of 120 °C, GP zones are the dominant matrix precipitates due to their lower nucleation activation energy[27]. Additionally, the high density of GP zones depletes Cu and Li in the matrix, delaying the nucleation of T_1 phases. Furthermore, lower atomic diffusion rates and shorter diffusion paths at lower aging temperatures lead to prolonged peak-hardness times and finer diameters of T_1 and GP zones. As the aging temperature increases, enhanced precipitation kinetics favor the formation of T_1 phases, which are thermodynamically more stable than θ' phases[42]. Concurrently, metastable GP zones transform into coarser θ' phases at elevated temperatures. This competitive relationship results in an increased number density of T_1 phases and a corresponding decrease in the number density of θ' phases. At 200 °C, the higher diffusion rates lead to a reduced nucleation rate but promote significant coarsening of T_1 phases. Consequently, the number density of T_1 phases decreases sharply, while their thickness increases

Table 2. The measured data of T_1 parameters in different TMT-treated alloys

Sample	T_1 (Al_2CuLi)			
	d **(nm)**	***t*** **(nm)**	***N*** **(10)**	f_v **(%)**
TMT-120	28 ± 3	1.30 ± 0.12	3.20 ± 0.13	0.51 ± 0.10
TMT-150	45 ± 4	1.32 ± 0.10	5.10 ± 0.22	2.16 ± 0.08
TMT-175	53 ± 5	1.65 ± 0.15	5.60 ± 0.20	4.07 ± 0.10
TMT-200	49 ± 8	2.42 ± 0.15	3.50 ± 0.22	3.22 ± 0.12

TMT: Thermo-mechanical treatment; *d*: average diameter; *t*: average thickness; *N*: number density; f_v: volume fraction.

Table 3. The measured data of θ' /GP parameters in different TMT-treated alloys

Sample	θ' (Al_2Cu) / GP zone			
	d **(nm)**	***t*** **(nm)**	***N*** **(10)**	f_v **(%)**
TMT-120	7 ± 1.5	0.34 ± 0.05	148 ± 6.5	0.19 ± 0.02
TMT-150	30 ± 2	1.84 ± 0.22	2.95 ± 0.20	0.38 ± 0.08
TMT-175	21 ± 5	1.94 ± 0.15	1.40 ± 0.25	0.09 ± 0.02
TMT-200	25 ± 8	2.65 ± 0.25	0.83 ± 0.18	0.11 ± 0.04

TMT: thermo-mechanical treatment; *d*: average diameter; *t*: average thickness; *N*: number density; f_v: volume fraction.

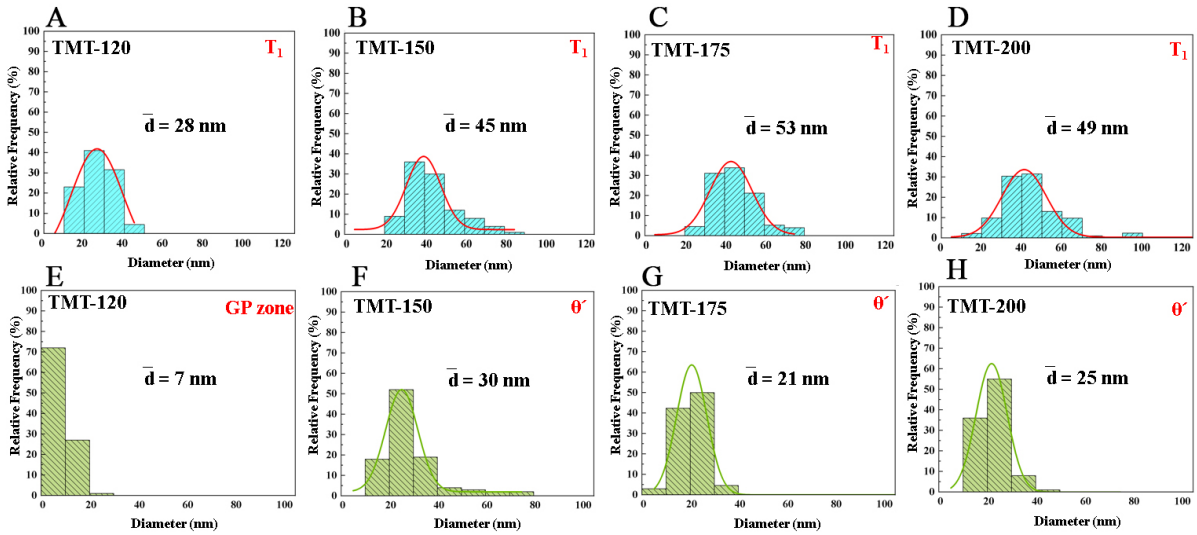

Figure 10. The statistical size distributions of precipitates at peak aging:(A and E) TMT-120; (B and F) TMT-150; (C and G) TMT-175; (D and H) TMT-200. TMT: Thermo-mechanical treatment.

notably [Figure 9]. The coarsening of T_1 phases is primarily driven by thickening normal to their planes, attributed to the long diffusion distances of Cu above 175 °C. This phenomenon is associated with the nucleation and lateral migration of ledges at the broad interfaces of T_1 phases, as previously reported by Wu *et al.*[33].

To further elucidate the influence of aging temperature, grain boundary precipitates (GBPs) were characterized to assess their precipitation behavior at GBs. Figure 11 presents typical HAADF-STEM images of sub-grain boundaries (sub-GBs) in the samples. The TMT-120 and TMT-150 samples exhibit a continuous and dense distribution of GBPs along their sub-GBs [Figure 11A and B]. Sub-GBs are primarily

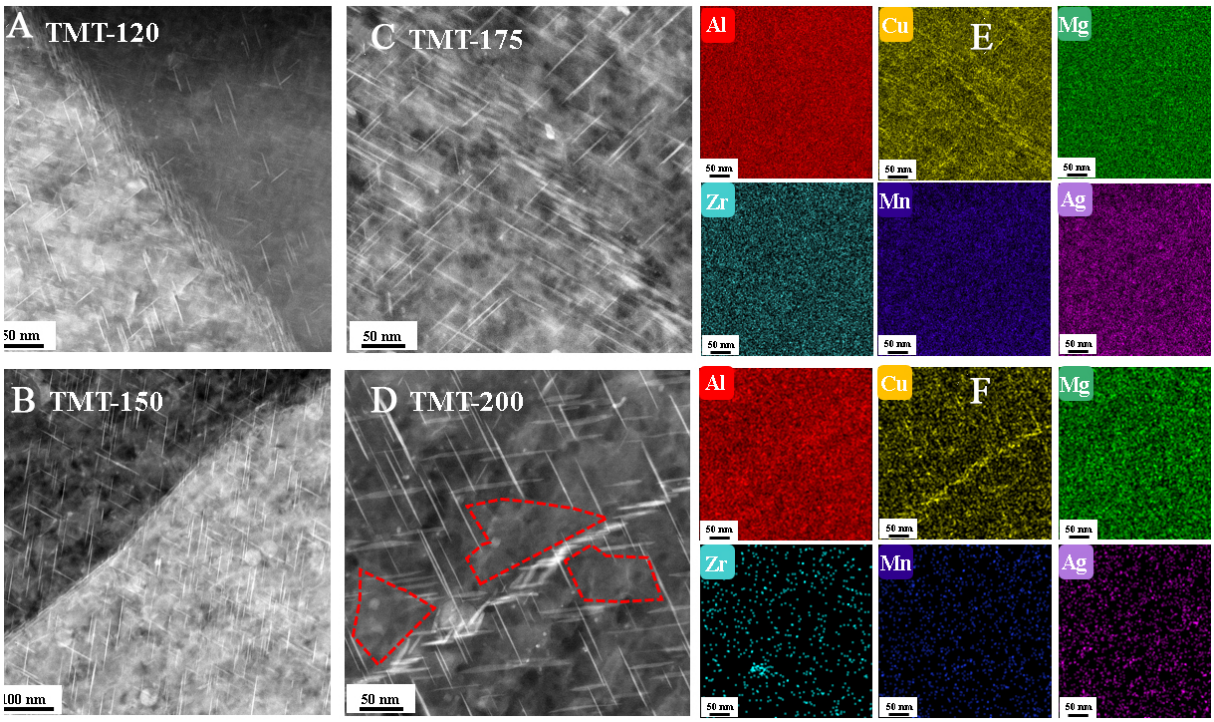

Figure 11. HAADF-STEM images along the $[110]_{Al}$ zone axis and corresponding EDS mappings of four TMT samples at sub-grain boundaries (A-D): (A) TMT-120; (B) TMT-150; (C) TMT-175; (D) TMT-200; (E) and (F) show the EDS analysis for (C) and (D), respectively. TMT: Thermo-mechanical treatment; HAADF-STEM: high-angle annular dark-field scanning transmission electron microscopy; EDS: X-ray spectroscopy.

identified as low angle grain boundaries (LAGBs) composed of entangled dislocations[43], which facilitate heterogeneous nucleation of precipitates within the grains. Solute atoms preferentially segregate near dislocation lines to reduce lattice distortion, forming Cottrell atmospheres[44]. Thus, sub-GBs formed by dislocations are suggested to promote T_1 precipitation. The heterogeneous nucleation of T_1 at sub-GBs is a critical feature of age-hardened Al-Cu-Li alloys, significantly influencing their mechanical properties. The GBP characteristics vary distinctly in peak-aged samples with increasing aging temperatures. At 175 °C, the TMT-175 sample demonstrates denser T_1 precipitates along sub-GBs, and the segregation of solute atoms in sub-GBs becomes more pronounced [Figure 11C]. EDS mapping reveals that GBPs in the TMT-175 sample primarily consist of Cu-rich precipitates with slight Ag enrichment [Figure 11E].

At an aging temperature of 200 °C, coarse, plate-like GBPs are observed in the TMT-200 sample [Figure 11D]. These GBPs, exhibiting plate or rod-like morphologies, are identified as T_2 or T_B phases. The elevated temperature promotes the aggregation of excess Cu atoms along sub-GBs, reducing the availability of Cu for matrix precipitation. The precipitation of these coarse equilibrium phases along sub-GBs continuously depletes Cu from adjacent regions, leading to localized solute depletion. As a result, the distribution of T_1 phases becomes non-uniform at the sub-GBs, as indicated by the red dashed line in Figure 11D.

Effect of aging temperature on mechanical properties

Figure 12A and B exhibits the engineering stress-strain curves of TMT samples in peak aging, while the corresponding YS, ultimate tensile strength (UTS), and EL values are summarized in Table 4. For comparison, the mechanical properties of the solution-treated and pre-aged samples are reported in our

Table 4. Tensile properties of different TMT samples

Sample	YS (MPa)	UTS (MPa)	EL (%)	PSE (GPa·%)
TMT-120	644 ± 9.5	680 ± 5.0	12.4 ± 0.8	8.4
TMT-150	705 ± 5.2	719 ± 1.8	11.8 ± 1.0	8.5
TMT-175	715 ± 7.9	724 ± 10.0	7.1 ± 1.5	5.1
TMT-200	656 ± 5.0	688 ± 7.8	7.4 ± 0.8	5.1

TMT: Thermo-mechanical treatment; YS: yield strength; UTS: ultimate tensile strength; EL: elongation; PSE: the product of strength and elongation to fracture.

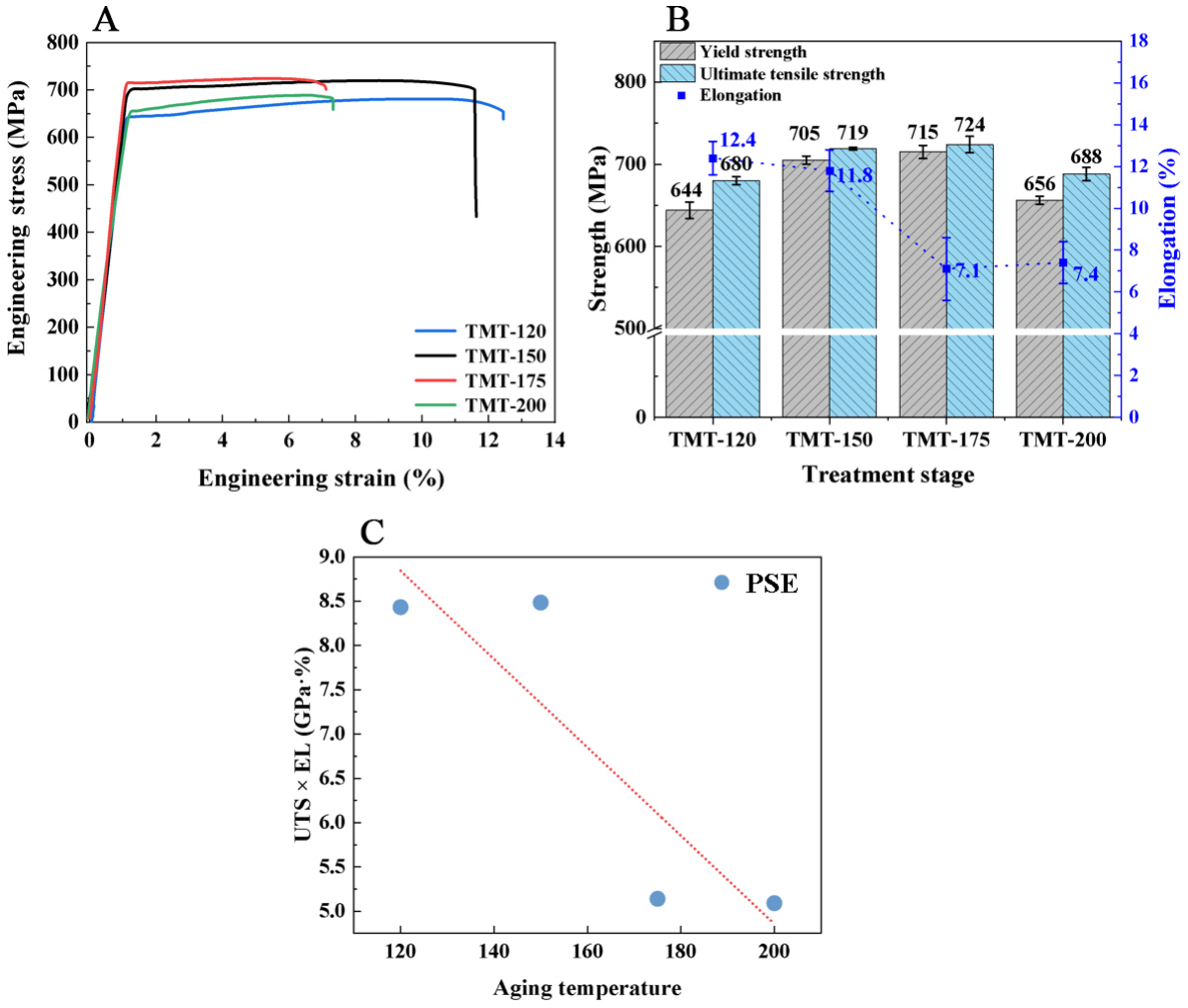

Figure 12. Engineering stress-strain curves (A) and the corresponding mechanical properties (B) of the peak-aged TMT samples; (C) is the PSE *vs.* aging temperature in this study. TMT: Thermo-mechanical treatment; PSE: the product of strength and elongation to fracture.

previous studies. Compared to the solution-treated sample (YS = 185 MPa, UTS = 386 MPa, EL = 14.4%), a progressive increase in YS from 644 MPa to 715 MPa is observed for TMT samples as the aging temperature rises from 120 °C to 175 °C. However, the EL correspondingly decreases from 12.4% to 7.1%. At 200 °C, further reductions in tensile strength are observed, with UTS, YS, and EL decreasing to 656 MPa, 688 MPa, and 7.4%, respectively. This trend highlights a negative correlation between aging temperature and ductility.

Figure 12C compares the products of strength and elongation (PSE) for different samples. The PSE serves as a comprehensive metric to evaluate the strength-ductility synergy and fracture toughness of metallic materials, with higher values indicating better performance and reduced failure risk[45]. Notably, the TMT-120 (8.43 GPa·%) and TMT-150 (8.48 GPa·%) samples exhibit significantly higher PSE values compared to TMT-175 (5.14 GPa·%) and TMT-200 (5.09 GPa·%). These results underscore the superior strength-ductility balance achieved at lower aging temperatures (120-150 °C).

To further analyze the differences in fracture behavior, Figure 13 shows fractographs of different TMT samples. The TMT-120 sample [Figure 13A] predominantly exhibits a typical transgranular ductile fracture mode, characterized by dense, deep dimples [Figure 13E] with minimal flat regions. The uneven fracture morphology of the TMT-120 sample demonstrates its superior deformation compatibility, reflecting its excellent plasticity (EL = 12.4%). The fracture surfaces of the TMT-150 samples [Figure 13B] show partially elongated grain morphologies, suggesting localized intergranular fracture initiation, while retaining dominant transgranular dimples, albeit with smaller dimples [Figure 13F] compared to the TMT-120 sample. In contrast, the TMT-175 [Figure 13C] and TMT-200 samples [Figure 13D] exhibit a higher proportion of intergranular fracture, characterized by distinct GBs [Figure 13G] and shallow dimples [Figure 13H], with nearly flat regions, indicating poor ductility. Figure 13I presents the BSE micrograph of the TMT-120 fracture surface. EDS analysis reveals that the particles are Al-Fe-Mn-Cu intermetallic compounds [Figure 13J and K], with slip bands radiating from the particle/matrix interfaces, indicating that these particles induce localized plastic deformation in the adjacent matrix, contributing to crack initiation.

In this work, the strengthening mechanism of the samples subjected to different TMT processes can be attributed to strain strengthening and precipitation strengthening, in addition to the intrinsic strength of Al and solution strengthening. Solution strengthening can be considered consistent since the solution treatment and pre-aging process are identical across all samples. Therefore, the mechanical properties of the TMT samples are primarily influenced by strain strengthening and precipitation strengthening. The contribution of the strain strengthening can be quantified using the Bailey-Hirsch relationship[46]:

$$\Delta\sigma_{\mathrm{d}} = M\alpha Gb\rho_d^{\frac{1}{2}} \tag{3}$$

Where M represents the Taylor factor (3.06), α is a constant between 0.2-0.5 (with a fitted value of 0.4 in this study), G is the shear modulus of Al matrix (26.9 GPa), b is the burgers vector (0.286 nm), and ρ_d is the dislocation density. Hence, the pre-stretching at 8% enhanced the strength by strain strengthening.

The precipitation strengthening mechanism associated with the shearable T_1 phases can be simplified as follows[47]:

$$\Delta\tau_{\mathrm{p}} \propto D^2 N^{\frac{1}{2}} t^{-\frac{3}{2}} \tag{4}$$

From Equation 4, it can be inferred that both the diameter (D) and the number density (N) of T_1 phases contribute positively to the increase in strength, with the effect of D on strength being more significant than that of N. However, an increase in the precipitate thickness (t) has a detrimental impact on strength. In terms of strain strengthening, the dislocation density gradually decreases as the aging temperature rises, attributed to the dislocation recovery during aging[27], resulting in a continuous reduction in strain strengthening from the TMT-120 to the TMT-200 samples. The highest YS (715 MPa) in the TMT-175 sample is attributed to the combination of the highest T_1 number density (3.2×10^{21} m^{-3}) and largest T_1 diameter (53 nm). In contrast, the relatively low YS (656 MPa) in the TMT-200 sample is a result of the

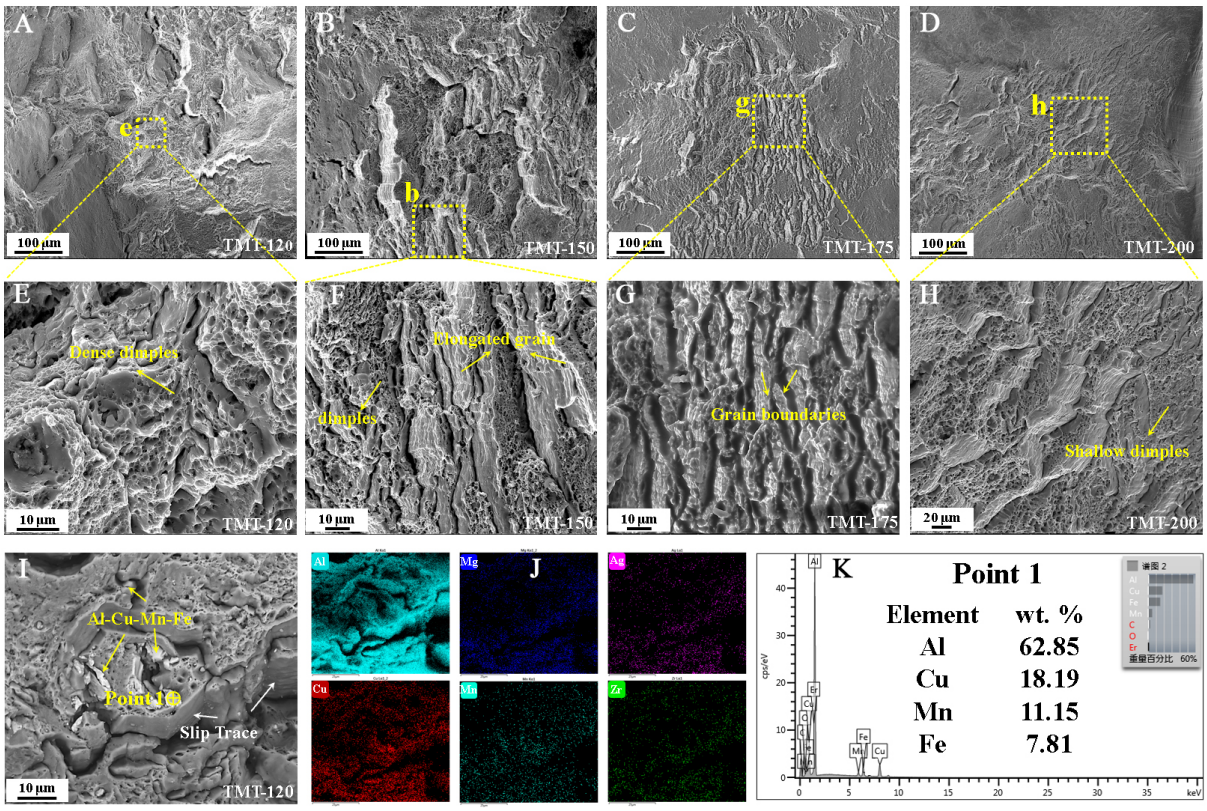

Figure 13. The fracture morphology of the different TMT samples: (A, E and I) TMT-120; (B and F) TMT-150; (C and G) TMT-175; (D and H) TMT-200; (E-H) are high-magnification images of the yellow dashed boxes in (A-D), respectively; (I) is the BSE image and the corresponding EDS analysis of theTMT-120 sample. TMT: thermo-mechanical treatment; BSE: backscattered electron detector; EDS: X-ray spectroscopy.

significantly coarsened T_1 precipitate thickness (2.44 nm) and the lowest dislocation density (0.83×10^{21} m^{-3}) in the matrix.

The ductility of the TMT samples is related to their ability to accumulate dislocations during deformation. Higher aging temperatures result in lower dislocation densities, thereby increasing the potential for dislocation accumulation[48]. This suggests that the TMT-175 and TMT-200 samples should exhibit a greater capacity for dislocation accumulation, which would, in turn, be expected to increase their corresponding EL. However, this prediction is inconsistent with the tensile test results shown in Figure 12A. When the aging temperature exceeds 175 °C, the EL decreases rapidly, indicating that dislocation recovery during aging does not fully control the EL. Instead, the presence of precipitates with varying sizes, types, and distributions within the matrix impedes dislocation slip, thereby affecting the capacity for dislocation accumulation. Therefore, the precipitate interacts with the moving dislocations, becoming the primary factor limiting ductility at elevated aging temperatures. Generally, brittle secondary phases often act as effective crack nucleation sites due to their tendency to preferentially fracture under tensile loading. The fracture strain (ε_f) of aluminum alloys can be expressed as follows[49]:

$$\varepsilon_f = \frac{1}{\bar{\varepsilon}(\theta)}\left[\frac{I}{0.405\pi h}\right]^{\frac{1}{n+1}}\left[\frac{\lambda_c}{2r_c}-1\right]^{\frac{1}{n+1}}\frac{\tilde{\varepsilon}}{2} \quad (5)$$

Where λ_c and r_c are the interparticle spacing and diameter of brittle particles, respectively, $\tilde{\varepsilon}(\theta)$ is the normalized coefficient, and I and h are functions of the strain hardening exponent (n). The term $\tilde{\varepsilon}$ represents the local plastic strain induced by microcracks. In Al-Cu-Li alloys, the presence of various precipitates or secondary phases creates deformation incompatibilities at matrix/precipitate interfaces, generating geometrically necessary dislocations (GNDs). These GNDs induce local plastic strain at the interfaces. When the GND density reaches a critical value (a constant in the Al matrix), fracture occurs within the matrix. The relationship between the a and the critical dislocation density ρ_g^c is given by[50]:

$$\tilde{\varepsilon} = 0.25 b \lambda_p \rho_g^c \tag{6}$$

Where b is the Burgers vector, and λ_p is the interparticle spacing of precipitates. Thus, any microstructural transformation that reduces λ_p of shear-resistant precipitates, such as an increase in precipitate volume fraction or diameter, will decrease $\tilde{\varepsilon}$, thereby impairing the alloy's plasticity. However, for shearable precipitates (metastable GP zones or small-sized T_1 phases), it is difficult to generate new dislocations around these precipitates, meaning that shearable precipitates do not deteriorate the alloy's plasticity.

As the aging temperature increases, Figure 14 exhibits a schematic showing the microstructure evolution and the precipitate-dislocation interaction in the various TMT samples during deformation. The precipitates in the TMT samples aged at 175 °C and 200 °C are primarily coarse T_1 phases [Figure 14C and D]. Zeng *et al.*[51] reported that the interaction between dislocations and the T_1 phase transitions from shearing to a by-passing mechanism when the T_1 phase exceeds 1.9 nm in thickness or 65 nm in diameter. In the TMT-200 sample [Figure 14H], pile-up dislocations are trapped by the dense and coarse T_1 phases, forming Orowan loops. This interaction promotes the formation of voids and, under high stress, leads to decohesion at the precipitate-matrix interface, resulting in premature failure. A similar precipitate-dislocation interaction mechanism has been observed for the shear-resistant θ' phase[27], further highlighting the structural incompatibility between shear-resistant precipitates and the matrix during deformation. Based on Equation 6, the presence of shear-resistant T_1 and θ' phase can significantly decrease the local plastic strain, consequently resulting in a deterioration in the plasticity of the TMT-175 and TMT-200 samples. In contrast, the dense and fine T_1 precipitates in the TMT-150 sample facilitate dislocation motion by shearing the T_1 phase [Figure 14B]. However, dislocations cannot shear the same T_1 precipitate multiple times at the same location[52], promoting more homogeneous plasticity across multiple slip systems [Figure 14F]. This minimizes strain localization and retards plastic instability, which accounts for the enhanced strength and ductility observed in the TMT-150 sample [Figure 12B]. For the TMT-120 sample aged at 120 °C, the metastable GP zones [Figure 14A], which exhibit the highest number density, are susceptible to shearing at various sites [Figure 14E][21,39]. Furthermore, the sparse T_1 precipitates contribute to strengthening the material by impeding dislocation movement and facilitating dislocation cross-slip, thus improving the strain hardening ability. The transfer of dislocation slip rather than dislocation accumulation on shearable GP zones is the primary factor contributing to the sustained plasticity of 12.4% in the TMT-120 sample.

On the other hand, pre-aging treatment before pre-stretching significantly enhances the alloy's plasticity. In the as-quenched alloy directly subjected to 8% pre-stretching, uniaxial tensile testing results in the formation of dislocation cells at the GBs [Figure 5D] due to the absence of precipitates in the as-quenched matrix that would hinder dislocation movement. During aging, these dislocation cells lead to an uneven precipitate distribution at the GBs, making these regions prone to plastic localization and causing deformation inconsistency between the matrix and GBs[53]. This, in turn, generates stress concentration, ultimately reducing the alloy's plasticity. In contrast, for the sample subjected to pre-aging at 110 °C, no

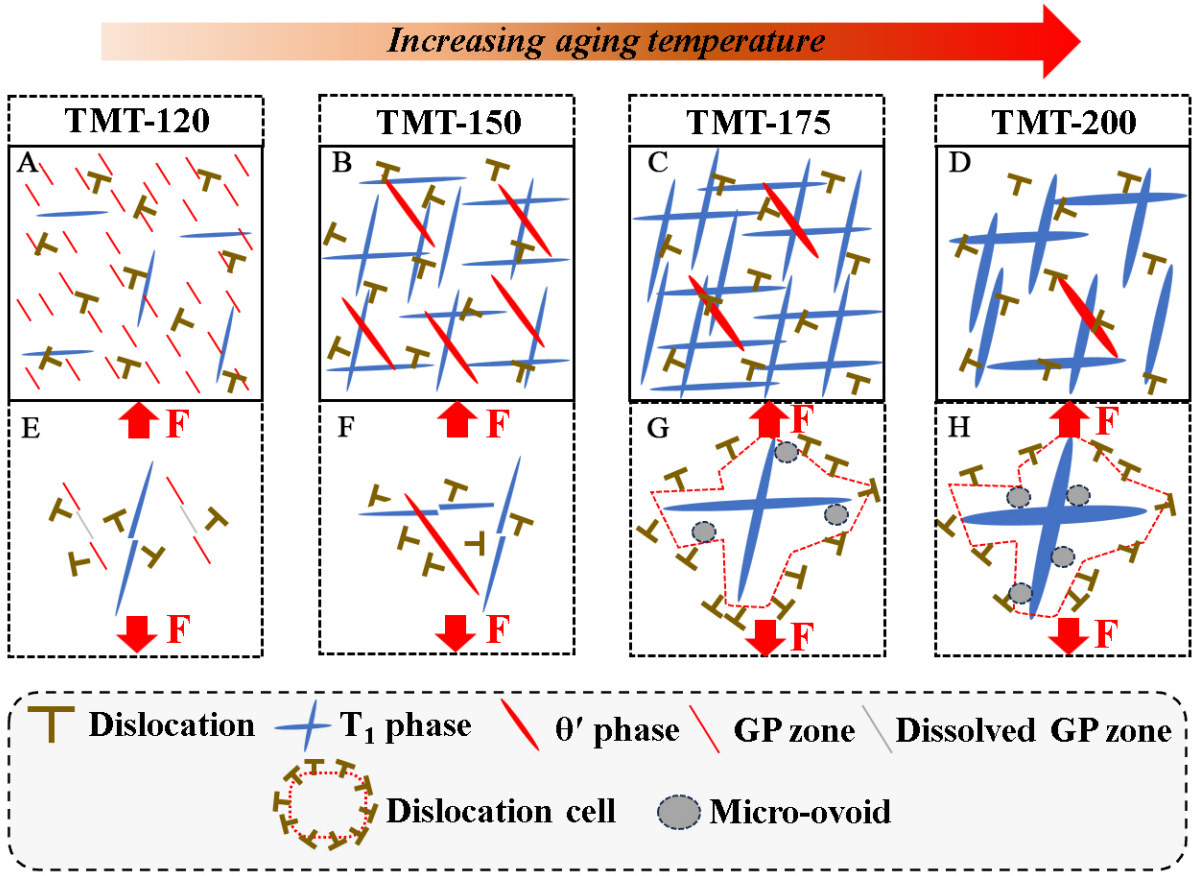

Figure 14. Schematic diagram showing the microstructure evolution with increasing aging temperature (A-D), and precipitate-dislocation interaction in the different TMT samples during deformation (E-H): TMT-120 sample (A and E); TMT-150 sample (B and F); TMT-175 sample (C and G); TMT-200 sample (D and H). TMT: Thermo-mechanical treatment.

significant dislocation tangling is observed at the GBs [Figure 5D]. This uniform dislocation structure promotes more homogeneous precipitation during aging, effectively reducing stress concentration and enhancing plasticity.

While the high dislocation density and precipitation strengthening greatly improve the strength of Al-Cu-Li alloys, careful control of the aging process is essential to prevent strength-ductility synergy from being compromised. Our findings demonstrate that pre-aging treatment promotes a high density of uniformly distributed dislocations, while subsequent aging effectively modulates the size, distribution, and number density of GP zones and T_1 phases, enabling them to be sheared by dislocations and thereby enhancing both strength and ductility. Nevertheless, it is difficult for dislocations to shear the coarse T_1 phase, which preserves strength but significantly reduces plasticity. Notably, TMT-120 samples, where the distribution of T_1 phases is influenced by the formation of GP zones and high-density dislocation, exhibit superior plasticity compared to TMT-150 samples, where the T_1 phase is regulated only by high dislocation density. An effective strategy for enhancing the strength-ductility synergy in Al-Cu-Li alloys is to develop precipitates with a high aspect ratio, high density, and shearability through aging treatment. Therefore, precise microstructural control over the amount, size, and distribution of coexisting GP zones and T_1 phases is essential for optimizing the mechanical performance of Al-Cu-Li alloys.

CONCLUSIONS

The effects of aging temperature on the precipitation behavior of T_1, θ', and GP zones, as well as the mechanical properties of Al-Cu-Li alloys, were systematically investigated through microstructural characterization, hardness measurements, and tensile testing. After solution treatment, a low-temperature pre-aging at 110 °C combined with 8% pre-stretching introduces a homogeneous, high-density dislocation configuration into the matrix, promoting a uniform distribution of precipitates. When the aging temperature exceeds 175 °C, the increased thickness of the T_1 precipitate hinders dislocation shearing, leading to a significant reduction in ductility at peak aging. Aging at 150 °C enhances the precipitation of dense T_1 phases, achieving an optimal balance between yield strength (705 MPa) and elongation (11.8%). In contrast, aging at 120 °C produces a microstructure characterized by the coexistence of dense GP zones and sparse T_1 precipitates, yielding the highest ductility (12.4%) among the peak-aged samples. These findings highlight the importance of modulating microstructure by precisely controlling the relative amount, size, and distribution of coexisting GP zones and T_1 phases to improve the strength-ductility balance in extruded Al-Cu-Li-Mg-Ag alloy.

DECLARATIONS

Authors' contributions

Conceptualization, investigation, writing - original draft: Xu, X.
Writing - review and editing: Tong, X.; Zhang, L.
Writing - review and editing, supervision, funding acquisition: Wu, G.

Availability of data and materials

The data supporting the findings of this study are available from the corresponding author upon reasonable request.

Financial support and sponsorship

This work was supported by the National Natural Science Foundation of China (No.52475380, 51871148, and 51821001).

Conflicts of interest

All authors declared that there are no conflicts of interest.

Ethical approval and consent to participate

Not applicable.

Consent for publication

Not applicable.

REFERENCES

1. Dursun, T.; Soutis, C. Recent developments in advanced aircraft aluminium alloys. *Mater. Des. (1980-2015).* **2014**, *56*, 862-71. DOI
2. Zhang, X.; Chen, Y.; Hu, J. Recent advances in the development of aerospace materials. *Prog. Aerosp. Sci.* **2018**, *97*, 22-34. DOI
3. Xie, Y.; Liu, S.; Guo, X.; He, X.; Liang, C.; Deng, Y. Modulation of precipitation behavior by dislocations and alloying for superior strength-ductility balance in Al-Cu-Li alloys. *J. Alloys. Compd.* **2025**, *1010*, 177334. DOI
4. Deng, S.; Liu, Z.; Zeng, G.; et al. The precipitation evolution and mechanical properties of an Al-Cu-Li-Mg alloy during natural aging. *J. Mater. Sci. Technol.* **2024**, *192*, 42-53. DOI
5. Yang, X.; Wang, J.; Xue, C.; et al. Enhancing strength and ductility of Al-Cu-Li alloys by microalloying both Er and Zr to promote

complete transformation from δ' (Al_3Li) to T_1 (Al_2CuLi) precipitates. *J. Mater. Res. Technol.* **2024**, *32*, 2913-30. DOI

6. Wang, L.; Zhan, S.; Ruan, Y.; Miao, T.; Hu, L. Influence of grain size on twinning behavior of WE43 magnesium alloy during room-temperature compression deformation. *J. Rare. Earths.* **2024**, *42*, 2285-92. DOI
7. Li, S.; Wang, Q.; Chen, J.; Wu, C. The effect of thermo-mechanical treatment on the formation of T1 phase and δ'/θ'/δ' composite precipitate in an Al-Cu-Li-Mg alloy. *Mater. Charact.* **2021**, *176*, 111123. DOI
8. Xu, X.; Wu, G.; Zhang, L.; et al. Effects of heat treatment and pre-stretching on the mechanical properties and microstructure evolution of extruded 2050 Al-Cu-Li alloy. *Mater. Sci. Eng:. A.* **2022**, *845*, 143236. DOI
9. Lv, P.; Wang, R.; Peng, C.; Cai, Z. Improved strength and ductility of rapidly solidified 2195 alloy by pre-rolling combined with double aging and interrupted aging. *Mater. Sci. Eng:. A.* **2023**, *873*, 145023. DOI
10. Xie, B.; Huang, L.; Xu, J.; et al. Effect of the aging process and pre-deformation on the precipitated phase and mechanical properties of 2195 Al-Li alloy. *Mater. Sci. Eng:. A.* **2022**, *832*, 142394. DOI
11. Wang, X.; Shao, W.; Jiang, J.; Li, G.; Wang, X.; Zhen, L. Quantitative analysis of the influences of pre-treatments on the microstructure evolution and mechanical properties during artificial ageing of an Al-Cu-Li-Mg-Ag alloy. *Mater. Sci. Eng:. A.* **2020**, *782*, 139253. DOI
12. Zou, Y.; Cao, L.; Wu, X.; Tang, S.; Guo, M. Synergetic effect of natural ageing and pre-stretching on the ageing behavior in T'/η' phase-strengthened Al-Zn-Mg-Cu alloys. *J. Mater. Sci. Technol.* **2023**, *146*, 240-51. DOI
13. Rodgers, B.; Prangnell, P. Quantification of the influence of increased pre-stretching on microstructure-strength relationships in the Al-Cu-Li alloy AA2195. *Acta. Materialia.* **2016**, *108*, 55-67. DOI
14. Huang, L.; He, L.; Li, S.; Liu, W.; Huang, J.; Chen, S. Effects of pre-stretch on microstructure, mechanical properties and corrosion resistance of 2A14 aluminum alloy. *Trans. Nonferrous. Met. Soc. China.* **2024**, *34*, 1065-80. DOI
15. Dai, W.; Jiang, Y.; Yao, J.; Wang, Y.; Cao, F. Simultaneously improving the strength and ductility of an Ag-free 2195 Al-Li alloy by T8 treatment with cryogenic pre-rolling. *J. Alloys. Compd.* **2024**, *976*, 173214. DOI
16. Dong, F.; Huang, S.; Yi, Y.; et al. Effect of increased stretching deformation at cryogenic temperature on the precipitation behavior and mechanical properties of 2060 Al-Li alloy. *Mater. Sci. Eng:. A.* **2022**, *834*, 142585. DOI
17. Xiao, Y.; Guo, A.; Cui, H.; Wang, Z.; Kong, C.; Yu, H. Microstructure evolution, mechanical response, and corrosion resistance for a 2195 Al-Li alloy under different rolling reductions during cryorolling. *J. Alloys. Compd.* **2024**, *997*, 174973. DOI
18. Xu, J.; Huang, L.; Xu, Y.; et al. Effect of pulsed electromagnetic field treatment on dislocation evolution and subsequent artificial aging behavior of 2195 Al-Li alloy. *Mater. Charact.* **2022**, *187*, 111872. DOI
19. Xie, B.; Huang, L.; Xu, J.; Wang, Y.; Li, J. Microstructure evolution and strengthening mechanism of Al-Li alloy during thermo-electromagnetic forming process. *J. Mater. Process. Technol.* **2023**, *315*, 117922. DOI
20. Xu, X.; Wu, G.; Tong, X.; et al. Enhancing strength-ductility synergy in an extruded Al-Cu-Li-Mg-Ag alloy via homogeneous GP zones and dislocation configuration. *Mater. . Des.* **2024**, *239*, 112766. DOI
21. Xu, X.; Wu, G.; Tong, X.; et al. Achieving superior strength-ductility balance by tailoring dislocation density and shearable GP zone of extruded Al-Cu-Li alloy. *Int. J. Plast.* **2024**, *182*, 104135. DOI
22. Li, S.; Duan, S.; Ming, W.; Wu, C.; Chen, J. Genetic structural phase evolution from Li-containing S-like phase precipitates towards S-phase in AlCuLiMg alloys. *Acta. Materialia.* **2022**, *233*, 117997. DOI
23. Xu, X.; Wu, G.; Zhang, L.; Tong, X. New insight into enhancing the comprehensive mechanical performance in non-stretched Al-Cu-Li-(Mg)-(Ag)-Mn-Zr alloys. *Mater. Lett.* **2024**, *360*, 135899. DOI
24. Chen, K.; Wu, X.; Cao, Y.; et al. Enhanced strength and ductility in an Al–Cu–Li alloy via long-term ageing. *Mater. Sci. Eng:. A.* **2021**, *811*, 141092. DOI
25. Chen, X.; Ma, X.; Xi, H.; Zhao, G.; Wang, Y.; Xu, X. Effects of heat treatment on the microstructure and mechanical properties of extruded 2196 Al-Cu-Li alloy. *MaterDes* **2020**, *192*, 108746. DOI
26. Costa Teixeira J, Cram D, Bourgeois L, Bastow T, Hill A, Hutchinson C. On the strengthening response of aluminum alloys containing shear-resistant plate-shaped precipitates. *Acta. Materialia.* **2008**, *56*, 6109-22. DOI
27. Yang, J.; Liu, C.; Ma, P.; Chen, L.; Zhan, L.; Yan, N. Superposed hardening from precipitates and dislocations enhances strength-ductility balance in Al-Cu alloy. *Int. J. Plast.* **2022**, *158*, 103413. DOI
28. Chen, B.; Liu, G.; Wang, R.; et al. Effect of interfacial solute segregation on ductile fracture of Al-Cu-Sc alloys. *Acta. Materialia.* **2013**, *61*, 1676-90. DOI
29. Cui, S.; Zhang, C.; Liu, M.; Chen, L.; Zhao, G. Precipitation behavior of an Al-Cu-Li-X alloy and competing relationships among precipitates at different aging temperatures. *Mater. Sci. Eng:. A.* **2021**, *814*, 141125. DOI
30. Liu, C.; Zhou, Y.; Ma, P.; He, J.; Chen, L. Enhanced age-hardening response at elevated temperature by natural-ageing-modified precipitation in an Al-Cu-Li-Mg alloy. *Mater. Charact.* **2023**, *199*, 112791. DOI
31. Allen, S. M. Foil thickness measurements from convergent-beam diffraction patterns. *Philos. Mag. A.* **1981**, *43*, 325-35. DOI
32. Dorin, T.; Donnadieu, P.; Chaix, J. M.; Lefebvre, W.; Geuser, F.; Deschamps, A. Size distribution and volume fraction of T_1 phase precipitates from TEM images: direct measurements and related correction. *Micron* **2015**, *78*, 19-27. DOI PubMed
33. Wu, M.; Liu, W.; Xiao, D.; Huang, L. Influence of thermal exposure on the microstructure evolution and mechanical behaviors of an Al-Cu-Li alloy. *Mater. Des.* **2023**, *227*, 111767. DOI
34. Tsivoulas, D.; Prangnell, P. The effect of Mn and Zr dispersoid-forming additions on recrystallization resistance in Al-Cu-Li AA2198 sheet. *Acta. Materialia.* **2014**, *77*, 1-16. DOI

35. Guo, Y.; Li, J.; Lu, D.; et al. Characterization of Al_3Zr precipitation via double-step homogenization and recrystallization behavior after subsequent deformation in 2195 Al-Li alloy. *Mater. Charact.* **2021**, *182*, 111549. DOI
36. Ivanov, R.; Deschamps, A.; De, G. F. Clustering kinetics during natural ageing of Al-Cu based alloys with (Mg, Li) additions. *Acta. Materialia.* **2018**, *157*, 186-95. DOI
37. Li, Z.; Ren, W.; Chen, H.; Nie, J. θ''' precipitate phase, GP zone clusters and their origin in Al-Cu alloys. *J. Alloys. Compd.* **2023**, *930*, 167396. DOI
38. Zhang, P.; Shi, K.; Bian, J.; et al. Solute cluster evolution during deformation and high strain hardening capability in naturally aged Al-Zn-Mg alloy. *Acta. Materialia.* **2021**, *207*, 116682. DOI
39. Chen, Y.; Weyland, M.; Hutchinson, C. The effect of interrupted aging on the yield strength and uniform elongation of precipitation-hardened Al alloys. *Acta. Materialia.* **2013**, *61*, 5877-94. DOI
40. Xu, X.; Wu, G.; Zhang, L.; et al. Regulation of precipitation behavior among T_1, S', and θ' phases in Al-Cu-Li-(Mg-Ag) alloys by optimizing Ag/Mg ratios. *Mater. Sci. Eng:. A.* **2023**, *876*, 145158. DOI
41. Dong, Y.; Ye, L.; Tang, J.; Liu, X.; Sun, Q. The effects of temperature on the creep-aging behavior and mechanical properties of AA2050-T34 alloy. *Mater. Sci. Eng:. A.* **2020**, *796*, 140010. DOI
42. Sun, J.; Wu, G.; Zhang, L.; Zhang, X.; Liu, L.; Zhang, J. Microstructure characteristics of an ultra-high strength extruded Al-4.7Cu-1Li-0.5Mg-0.1Zr-1Zn alloy during heat treatment. *J. Alloys. Compd.* **2020**, *813*, 152216. DOI
43. Ott, N.; Kairy, S. K.; Yan, Y.; Birbilis, N. Evolution of grain boundary precipitates in an Al-Cu-Li Alloy during aging. *Metall. Mater. Trans. A.* **2017**, *48*, 51-6. DOI
44. Jiang, L.; Li, J. K.; Cheng, P. M.; et al. Microalloying ultrafine grained Al alloys with enhanced ductility. *Sci. Rep.* **2014**, *4*, 3605. DOI PubMed PMC
45. Lin, J.; Fu, P.; Wang, Y.; et al. Effect of La addition on microstructure, mechanical behavior, strengthening and toughening mechanisms of cast Mg-Gd-Zn alloy. *Mater. Sci. Eng:. A.* **2023**, *866*, 144688. DOI
46. Bailey, J. E.; Hirsch, P. B. The dislocation distribution, flow stress, and stored energy in cold-worked polycrystalline silver. *Philos. Mag.* **1960**, *5*, 485-97. DOI
47. Dorin, T.; Deschamps, A.; Geuser, F. D.; Sigli, C. Quantification and modelling of the microstructure/strength relationship by tailoring the morphological parameters of the T1 phase in an Al-Cu-Li alloy. *Acta. Materialia.* **2014**, *75*, 134-46. DOI
48. Huang, Y.; Chen, Z.; Zheng, Z. A conventional thermo-mechanical process of Al-Cu-Mg alloy for increasing ductility while maintaining high strength. *Scripta. Materialia.* **2011**, *64*, 382-5. DOI
49. Chan, K. A fracture model for hydride-induced embrittlement. *Acta. Metallurgica. et. Materialia.* **1995**, *43*, 4325-35. DOI
50. Ashby, M. F. The deformation of plastically non-homogeneous materials. *Philos. Mag-J. Theor. Exp. Appl. Phys.* **1970**, *21*, 399-424. DOI
51. Zeng, G.; Li, H.; Deng, S.; et al. Detailed investigation on microstructure and strengthening contribution of Al-*x*Cu-1.3Li-X alloy sheets. *Mater. Charact.* **2023**, *205*, 113278. DOI
52. Deschamps, A.; Decreus, B.; De, G. F.; Dorin, T.; Weyland, M. The influence of precipitation on plastic deformation of Al-Cu-Li alloys. *Acta. Materialia.* **2013**, *61*, 4010-21. DOI
53. Noell, P. J.; Carroll, J. D.; Boyce, B. L. The mechanisms of ductile rupture. *Acta. Materialia.* **2018**, *161*, 83-98. DOI